Available online at www.sciencedirect.com
ScienceDirect
Advances in Space Research xxx (2009) xxx–xxx
ADVANCES IN SPACE RESEARCH (a COSPAR publication)
www.elsevier.com/locate/asr

Solar irradiance forecast and far-side imaging

J.M. Fontenla [a,*], E. Quémerais [b], I. González Hernández [c], C. Lindsey [d], M. Haberreiter [a]

[a] Laboratory for Atmospheric and Space Physics, University of Colorado, 1234 Innovation Drive, Boulder, CO 80303, USA
[b] UVSQ-IPSL, LATMOS-CNRS, réduit de Verriéres, BP3 91371, Verriéres le Buisson, France
[c] National Solar Observatory, Tucson, 950 N. Cherry Avenue, AZ 85719, USA
[d] CORA-North West Research Associates, 3380 Mitchell Ln., Boulder, CO 80301, USA

Received 1 December 2008; received in revised form 3 April 2009; accepted 7 April 2009

Abstract

This paper presents a new approach to forecasting short-term Lyα solar irradiance variations due to the presence and evolution of magnetically heated regions in the Sun's outer atmosphere. This scheme is based on images of the solar disk at key wavelengths, currently Ca II K filtergrams, maps of backscattered solar Lyα from the interplanetary medium, and helioseismic images of large far-side active regions. The combination of these resources allows accurate forecasts of the UV solar irradiance several days in advance. The technique takes into consideration the evolution of recently observed activity on the Sun's near surface as well as active regions on the Sun's far side. The far-side helioseismic maps and the Lyα backscattering are very important, because of the long period of time features spend on the Sun's far side compared with their typical evolution time and their relatively sudden appearance on the near side. We describe the basics of the forecasting technique and apply it to a case study that shows how the technique dramatically improves Lyα irradiance forecasting. An extension of the technique described here promises realistic forecasts of the entire FUV/EUV solar spectral irradiance spectrum.

Keywords: Forecast; Irradiance; Lyman-alpha

1. Introduction

Forecasting solar EUV and FUV irradiance necessary for feeding the thermospheric-chemistry and heating models and producing forecasts of the neutral and ion density in the Earth's upper atmospheric layers has been a long standing problem. Changes in the irradiance due to magnetic activity on the surface of the Sun are important over solar-cycle time scales and drive 11-year variations of the thermospheric neutral density (e.g., Fuller-Rowell et al., 2004). Also, short-term spectral irradiance changes at XUV/EUV/FUV wavelengths due to near-side active regions have very significant effects on the thermosphere. UV solar irradiance variations are believed to be mostly the result of active regions, which emit much more UV radiation than the quiet Sun. Short-term variations of UV irradiance at the Earth are the mostly result of (1) active region evolution, and (2) rotational modulation of active-region radiances even if these would have been unchanging in a non-rotating Sun.

The simplest forecast method is based on assuming that the features on the solar surface do not change but only rotate with the Sun. However, large unexpected variations are very often observed due to sudden, unpredictable emergence and rapid evolution of large active regions on the Sun's visible hemisphere. A further problem for short-term forecasting has been to account for large, fully developed active regions on the Sun's far hemisphere about to rotate into direct view.

Hydrogen atoms in the ~3-AU interplanetary medium act like a projector screen reflecting back to the Earth Lyα photons that originated on the Sun. Based on this backscatter signature, Quémerais and Bertaux (2000) have

* Corresponding author. Tel.: +1 303 735 3730.
E-mail address: juan.fontenla@lasp.colorado.edu (J.M. Fontenla).

0273-1177/$36.00 © 2009 COSPAR. Published by Elsevier Ltd. All rights reserved.
doi:10.1016/j.asr.2009.04.010

developed a method of forecasting the solar UV flux at the Earth. This method uses maps of the interplanetary background obtained by the SWAN/SOHO UV photometer (Quémerais and Bertaux, 2000; Quémerais et al., 2006) to account for active regions on the Sun's far hemisphere. The main weakness of backscatter diagnostics is a relative coarse spatial resolution and therefore temporal resolution, the former being a considerable fraction of a hemisphere and the latter several days.

In this paper we describe a new method that improves upon the previous technique by combining observations of the visible solar disk with both Lyα-backscatter maps and helioseismic images of large active regions on the Sun's far side. The combination of these three resources facilitates a forecast that previous methods cannot match. By combining previous knowledge of the distribution and evolution of active regions (Fontenla and Harder, 2005) and network with up-to-date far-side helioseismic imaging (Lindsey and Braun, 2000a), we can evaluate the emergence, growth, and decay of active regions with the local discrimination needed for a more realistic forecast. Then, by using the Lyα-backscatter observations we can further refine our knowledge of the Lyα brightness of previously-observed and newly-emerged features up to the point where a significantly improved forecast of the Lyα solar irradiance is accomplished.

High-quality measurements of the solar FUV (and longer wavelengths) irradiance are made by earth-orbiting SORCE/SOLSTICE (McClintock et al., 2005; Snow et al., 2005). These measurements are used to compare our forecasts with actual UV irradiance variations in the forecast period.

In Sections 2–4, we describe the method in detail. In Section 5, we apply it to a case study that shows how the contributions of various active regions change over a solar rotation and produce a time-dependence in the Lyα irradiance at 1 AU that could not be accurately forecast from near side or from Lyα-backscatter observations alone.

2. Synoptic maps of solar surface features

In our method, the state of the visible solar surface is described by a daily map of features present at each position on the solar disk. These are derived from daily full-disk observations by the Precision Solar Photometric Telescope (PSPT) at the Mauna Loa Solar Observatory (MLSO) available at http://lasp.colorado.edu/pspt_access (see Rast et al., 2008; Ortiz and Rast, 2008). We currently use the images from the PSPT Ca II K-line (~0.23 nm bandpass centered at 393.4 nm) and in the continuum at 606.0 nm. The procedure for this is described by Fontenla et al. (1999) and Fontenla and Harder (2005).

Fig. 1 shows an example of a daily-features map. A seven-letter code, shown in Table 1 has been devised to designate the solar surface features.

Using disk maps from previous days, the distribution of features on the invisible hemisphere is reconstructed and

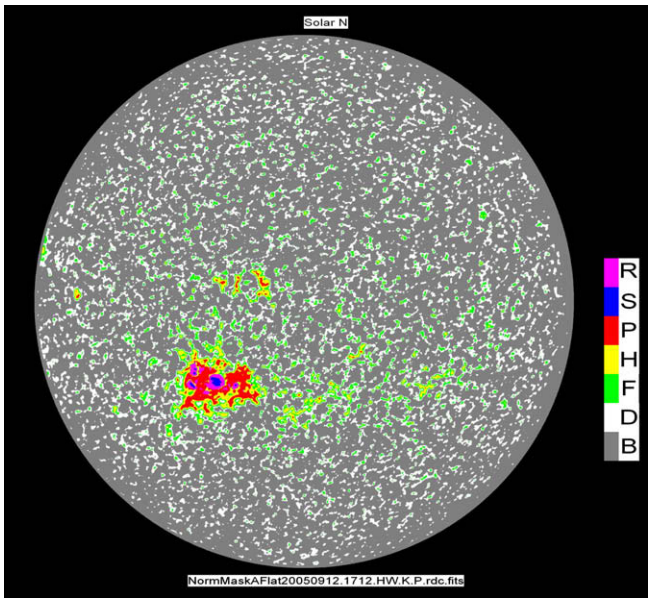

Fig. 1. Disk map on 2005/9/12 obtained from MLSO PSPT data. The letter codes are identified in Table 1.

mapped. However, the part of this map that is not currently visible may no longer be accurate. Thus, along with the synoptic map of the entire solar surface, we produce a corresponding *obsolescence map* describing how much time has elapsed since every portion of the Sun has been last observed. Observation of features close to the limb is problematic and does not produce accurate feature identification; therefore we do not consider regions with $\mu < 0.1$, where $\mu = \cos(\theta)$ and θ is the angle between the line of sight and the solar radial direction. When possible, we fill these locations with the most recent available data. However, we only consider a 30-day window before the nominal time of the synoptic map. Pixels for which no data were available in this temporal window (e.g., the poles) are classified with the letter "U" (black in both feature and obsolescence maps). We will eventually assume that such regions have a distribution of features typical of the quiet Sun, bearing in mind that the poles make little difference in the solar flux at the Earth.

Fig. 2 shows an example of such a map, with its associated obsolescence map. The synoptic map is created for a fixed grid in latitude and longitude, which currently has

Table 1
Codes of solar surface features.

Letter code	Color code	Feature description
B	Gray	Network cell center
D	White	Network lane
F	Green	Enhanced (or active) network
H	Yellow	Plage that is not faculae (i.e. not visible in white light)
P	Red	Facula (i.e. visible in white light when not far from the limb)
S	Blue	Sunspot umbra
R	Magenta	Sunspot penumbra
U	Black	Unobserved

Please cite this article in press as: Fontenla, J.M., et al. Solar irradiance forecast and far-side imaging. J. Adv. Space Res. (2009), doi:10.1016/j.asr.2009.04.010

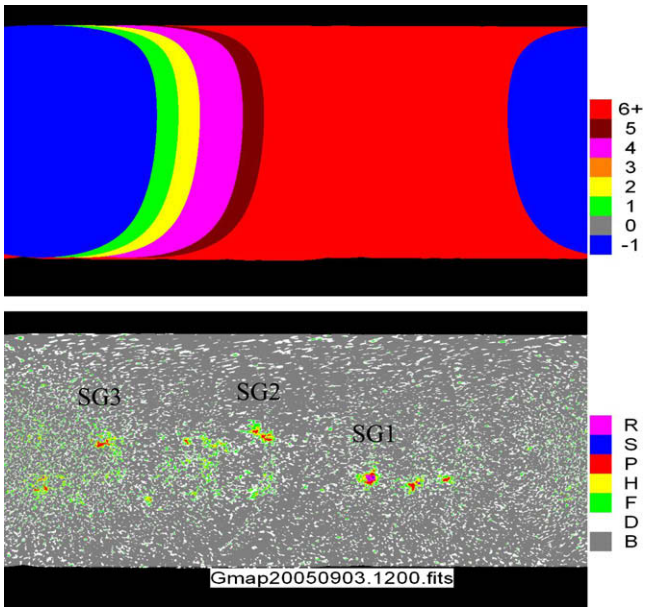

Fig. 2. Synoptic map on 2005/9/3 showing several relevant active regions. (Top) Obsolescence map showing the number of days since each pixel was last well observed from the Earth (at a position with $\mu > 0.1$); the number −1 indicates areas observed between 12:00 UT of the previous day and 12:00 UT of the nominal day of the synoptic map. (Bottom) Unrefined synoptic map showing the state of SG1 when it left the solar disk and other areas of the solar surface more recently observed. The black pixels, near the poles, are never well observed in our 30 days window. The letter codes are the same as in Fig. 1 and are identified in Table 1.

pixels of 0.25° × 0.25°. The PSPT images have higher resolution than the resolution we adopted for the synoptic maps. For irradiance forecasts, fine detail is important only for statistical purposes. When constructing a synoptic map, each pixel in the map is assigned the classification of that pixel derived from the most recent observation.

Synoptic maps encompass regions that have not been observed for several days (obsolescence >0 days). These parts of the map need to be improved, because the features in them have evolved. The behavior of old plage and active network follows patterns of decay, fragmentation, and fragments spread over several solar rotations. Often plage and active network result from decayed active regions with sunspots, but sometimes ephemeral regions appear that are not related to strong active regions. All this behavior has been described in the literature (e.g., Bumba and Howard, 1965). The ephemeral features do not produce large changes in irradiance but form an important overall background that can be approximately described by the most recent synoptic maps. In contrast with the more or less predictable behavior of old plage and active network, strong submerged active regions can emerge suddenly and evolve rapidly, within hours, or gradually and slowly, over many days. Young, strong active regions are unpredictable, and are responsible for the largest XUV/EUV/UV solar irradiance variations on short time scales. Consequently, it is critically important to be apprised of these as they become relevant for irradiance-forecasting purposes.

As the Sun rotates, active regions hidden on the Sun's far hemisphere may come into direct view. Since some areas of the far side have not been observed for many days (∼13), fast evolving strong active regions may emerge or die completely while on the invisible hemisphere. These situations lead to major, unexpected changes in the XUV/EUV/UV irradiance at the Earth with respect to the observed modulation in the previous solar rotation periods. Hence, synoptic maps based on direct observations are, by themselves, insufficient to produce accurate solar irradiance forecasts.

3. Helioseismic far-side data and active region changes

Helioseismic holography, a technique in local helioseismology developed by Lindsey and Braun (1997), has made it possible to monitor active regions on the Sun's far hemisphere (Lindsey and Braun, 2000a). This technique allows us to track large active regions on the Sun's far side before they rotate into direct view from the Earth. The technique is based on the travel time delay between acoustic waves going in and out of a magnetic region (Braun et al., 1988). Large active regions leave a phase signature in medium-degree p-modes that travel completely through the Sun with very little loss of coherence. Waves signatures observed on the near surface of the Sun are analyzed using "phase-sensitive helioseismic holography," to map the distribution of magnetic regions in the far hemisphere. For a detailed explanation of the method see Lindsey and Braun (2000b).

Both the Michelson Doppler Imager and the Global Oscillation Network Group (GONG) far-side imaging programs calculate maps of far-side activity on a daily basis that are available on respective websites. In a recent work, González Hernández et al. (2007) describe the relationship between the seismic signatures of the active regions in synoptic far-side maps and the average magnetic field strength and size of the associated feature when they are visible on the front side. This development allows for the calibration of the far-side seismic maps in terms of familiar characteristics of the active regions.

Our forecasting technique uses a series of far-side maps calculated from the GONG far-side monitor calibrated with a modified version of González Hernández et al. (2007) to update our obsolescent appraisal of regions that have rotated to the far hemisphere. Examples from such a series are shown in Fig. 3. These show a conspicuous growth of SG1 during its far-side transit between rotations 2033 and 2034, from a region whose seismic signature was marginally significant at the beginning of its far-side transit to a strong NOAA 10808 as it transited the east limb in solar rotation 2034. Our forecasting method uses the helioseismic images to update our appraisal of activity in the obsolete sectors of our synoptic maps. This includes the facility to insert new active regions into the synoptic maps when our first indication of these is a strong far-side seismic signature.

Please cite this article in press as: Fontenla, J.M., et al. Solar irradiance forecast and far-side imaging. J. Adv. Space Res. (2009), doi:10.1016/j.asr.2009.04.010

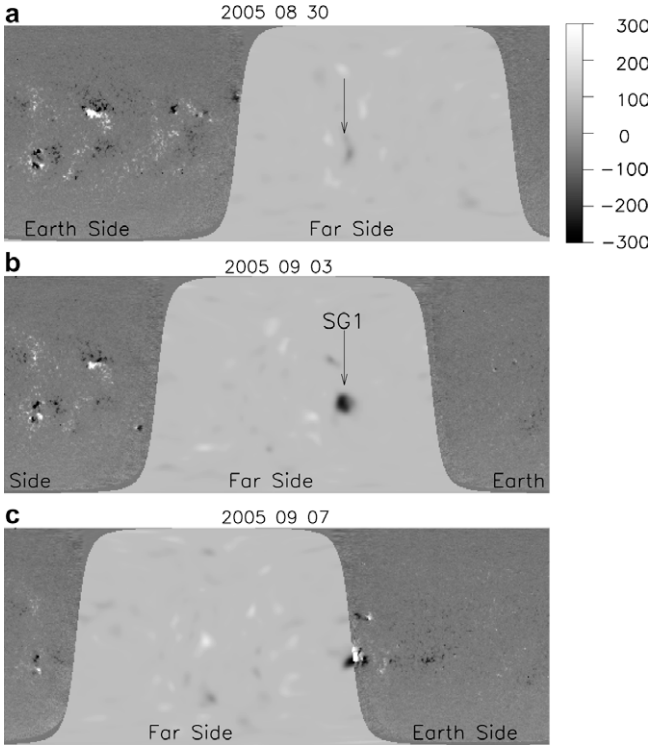

Fig. 3. GONG seismic images of the Sun's far surface on 2005/8/30, 2005/9/3 and 2005/9/7 are superimposed on concurrent GONG line-of-sight magnetograms of the near surface. The rapid growth of active region SG1 is evident by its greatly increased helioseismic signature in the middle frame, maintained as the region crosses the east limb (bottom frame). The gray scale to the right of the top frame renders the line-of-sight magnetic field in Gauss.

4. Lyα far-side backscattering and active region brightness

The SWAN (Solar Wind Anisotropies) instrument is a Lyman-alpha photometer on-board the SOHO mission and is dedicated to the study of the interplanetary UV background (Bertaux et al., 1995). The spacecraft was launched in December 1995 to study the Sun and the inner heliosphere. This mission is the result of an ESA-NASA cooperation and operations are expected to continue until 2013.

The interplanetary UV background is caused by the backscattering of solar Lyα photons by hydrogen atoms present in the inner heliosphere. This phenomenon was first observed in 1969 by two instruments on board the OGO-5 spacecraft (Bertaux and Blamont, 1971; Thomas and Krassa, 1971). The SWAN instrument is composed of two identical units placed on opposite sides of the SOHO spacecraft. Each unit is equipped with a periscope system which covers half of the sky. The instantaneous field of view is $5° \times 5°$ divided in 25 $1° \times 1°$ pixels. It takes roughly 24 h for each unit to make an image of the hemisphere it is facing. A full image (4π sr) is then obtained by putting both half images together. Between early 1996 and 2006, the SWAN instrument was making full-sky images at the rate of 4 per week. Since 2007, the SOHO observation program has been simplified and SWAN builds a map every day, i.e. 7 maps per week.

Fig. 4 shows two typical SWAN background maps. Quémerais and Bertaux (2000) showed that solar Lyα flux maps can be derived from such images by extracting the solar rotational modulation from the interplanetary background measurements. The low frequency modulation with a period of one year is due to the revolution of the spacecraft around the Sun. Other variations on different timescales result from the change in the ionization rates from the Sun due to solar EUV photo-ionizing flux and charge-exchange with solar wind protons. The interpretation of the SWAN observations requires careful analysis to disentangle the various processes affecting the raw images. For the present application, we use a modified version of the initial scheme developed by Quémerais and Bertaux (2000). In this scheme SWAN maps are initially computed in ecliptic coordinates from the raw observations for a period of one year before the date of the map. Then for each direction of sight in ecliptic coordinates, the one-year modulation and effects in the change of ionization are fitted by the following function:

$$I(t) = A\cos(\omega(t - t_0) + \phi) + B + C(t - t_0) \quad (1)$$

where $t - t_0$ is the elapsed time and $\omega = 2\pi/(1\text{ year})$. It has been verified that this empirical model, in which the mean temporal variation of the Sun over one year is included in the term $C(t - t_0)$, represents well the observed variations of the interplanetary background over a one-year period. In our processing, the $1° \times 1°$-resolution images are remapped onto a $4° \times 4°$ grid in Carrington coordinates. Then certain areas are eliminated from the analysis because they correspond to data gaps, mainly due to the shadow of the spacecraft and the sunshield which protects the instrument from direct sunlight. Hot stars in the Milky Way that mask the interplanetary medium backscattering also have to be removed from the data. This creates significant blind spots in the backscatter observations. The resulting maps are interpreted in terms of the solar source of the backscattered radiation. For this we utilize the solar surface synoptic maps, updated by the helioseismic observations, to compute the illuminating Lyα flux and the expected backscattering under that illumination. The comparison of the computed backscattering with the processed SWAN map shows which differences arise, and permits us to derive and implement corrections to the solar surface synoptic maps that minimize the difference between computed and observed Lyα backscattering.

5. A case study of forecasted Lyα irradiance

For the present comparison we selected the period covering the last half of 2005, during which very good data are available in all data sets and when significant activity was present on the disk despite being somewhat late in solar cycle 23. The observations we use are from the MLSO PSPT, the GONG, and the SWAN for the period from July to November 2005.

Please cite this article in press as: Fontenla, J.M., et al. Solar irradiance forecast and far-side imaging. J. Adv. Space Res. (2009), doi:10.1016/j.asr.2009.04.010

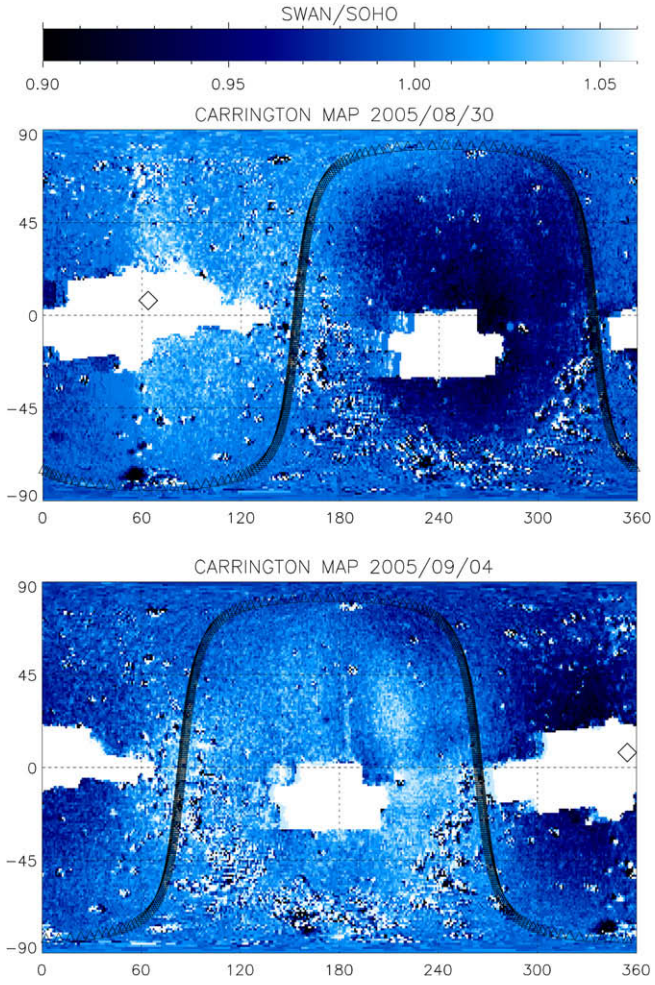

Fig. 4. Lyα backscattered flux measured by SWAN. The panels show the region SG1 before (top) and after (bottom) it suddenly developed.

5.1. Synoptic maps

For the Ca II K-line synoptic maps chosen in this case study, we refer back to Fig. 2 in Section 2. This map shows several active regions at different times. While different NOAA numbers are assigned in every rotation, we track active regions across the far side using helioseismic and Lyα-backscatter images, and for this reason we designate the active regions by our own notation to avoid the confusion of having two or more different active region numbers for the same solar feature.

During August–September 2005, we recognize three major active regions, labeled as SG1–SG3 in Fig. 2. Table 2 lists the main location and evolution characteristics of these active regions as they were observed at and before the date of this synoptic map.

Particularly interesting is the SG1 sunspot group. This was identified as NOAA 10797 when it rotated to the far side on 2005/8/30, and returned to the visible hemisphere in 2005/9/7–8 as NOAA 10808. This sunspot group was associated with several C- and M-class (up to M5.6) flares before first leaving the visible hemisphere. While on the far side, the group suddenly increased its helioseismic and Lyα backscatter signatures over the course of 3 days, and then decayed very slowly. As it returned to the visible solar disk the increased activity of this region was evident by the X17 limb flare it produced, apart from other M flares, see http://www.solarmonitor.org/region.php-?date=20050823&region=10797 and http://www.solarmonitor.org/-index.php?date=20050908. Regions SG2 and SG3 correspond to NOAA 10800 and 10801, respectively, after they reappeared in the visible hemisphere.

Table 2
Active region location, size, and growth.

Designation	Carrington coordinates		Width (°)	Height (°)	Growth/duration
	Longitude (°)	Latitude (°)			
SG1	226	−10.5	27	21	3/(3 days)
SG2	168	+16.5	24	15	1.5/(6 days)
SG3	60	+11.0	21	18	0.625/(4 days)

5.2. Forecast and refinement of synoptic-map features

The refinement of the obsolete part of the synoptic map shown in Fig. 2 is performed by examining the GONG helioseismic and SWAN backscattering data. These data indicate that the region SG1 grew rapidly between 2005/8/30 and 2005/9/3 while transiting the far side. Fig. 5 shows the time sequence of the increase in Lyα backscattered intensity at a position in the sky that would be most illuminated by SG1. However, the position is not very precise from SWAN because of the intrinsic defocusing of the backscattering process and the collimation characteristics (i.e. center-to-limb-variation) of the radiance from the surface features. Despite of these limitations, the backscattering data permits us to characterize the Lyα brightness

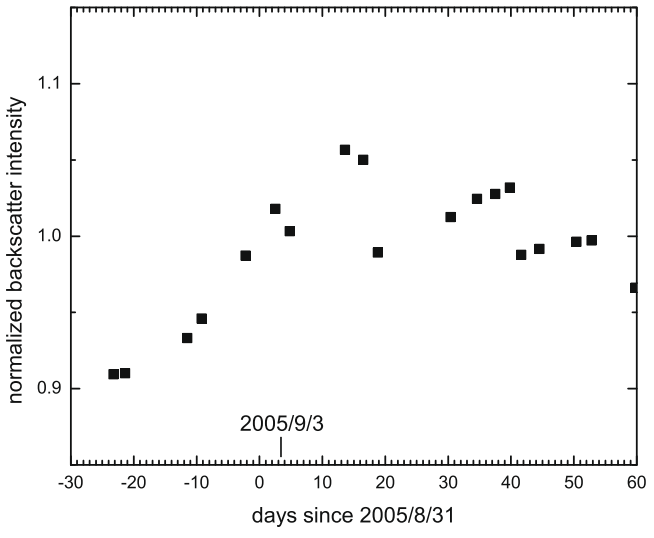

Fig. 5. Light curve of Lyα backscatter from the interplanetary medium radially extended from Carrington coordinates, $L = 230°$, $B = -13°$, those of SG1 in Fig. 2. This curve shows a rapid increase in Ly flux due to the growth of SG1 around 2005/9/1.

change of SG1, SG2, and SG3, as we show later in this section.

Fig. 3 shows the change in the helioseismic signature between these two dates and permits us to unequivocally identify SG1 as the main source of the increases observed in the backscattering plotted in Fig. 5. SG2 and SG3 have insignificant signatures in the helioseismic maps, and therefore their behavior cannot be assessed from helioseismology alone. However, as shown in Table 2, these regions had a known behavior while they were visible on the solar disk on or before 2005/9/3 and a somewhat modified extrapolated behavior explains well the SWAN observations.

The data from helioseismology shows a variation by a factor of about 10 in the calibrated helioseismic signature (corresponding to magnetic flux) over a $10° \times 10°$ area that corresponds to SG1. By trial and error we find that an increase in the active-region area by a factor of 3 would be necessary to explain the change in backscattering between 2005/8/30 and 2005/9/3. To refine the synoptic map shown in Fig. 2, we first select rectangular regions that encompass the major active regions. The location of their centers are listed for each active region in columns 2 and 3 in Table 2, with dimensions listed in columns 3 and 4. For each active region, we determine from the original synoptic map (Fig. 2), the area of the sunspot umbra, penumbra, facula and plage (features S, R, P, and H, respectively) within its respective rectangle. We then replace the interior of each rectangle with an idealized active region whose components are a single circular umbra, S, surrounded by concentric annuli representing penumbra, R, facula, P, and plage, H, in the order of increasing radius. The area of each component in the rectangle is modified from that of its counterpart in the original synoptic image by multiplying the enhancement factor expressed in column 6 of Table 2. The content of the rectangle outside of the circular components is inhabited by inter-network and quiet and enhanced network (B, D, and F) in proportions appropriate for the original synoptic map.

For the purpose of comparing the predicted with the observed Lyα backscattering we assume the unobserved areas around the poles are filled with the quiet Sun mix of inter-network and network features. In this way we obtain predicted backscattering at high latitudes that are comparable to those in the SWAN data. (Note that because of all the planets, bright stars, and Sun itself in the ecliptic plane, we have to use SWAN data corresponding to latitudes that are affected by the poles.)

Using the synoptic map, we compute the Lyα flux emitted in all directions and thereby the backscattered signature that the altered synoptic map would produce. By comparing the computed backscatter with the SWAN observations, we determine correction factors to the feature areas that result from the previous refinement procedure, and apply them to further refine the synoptic maps just described. In this way we determined the final area factors that best match the SWAN observations. For the case of SG1, we find a growth factor of 2.8 between 2005/9/30 and 2005/9/4. The resulting refined synoptic map is shown in Fig. 6, representing activity as forecast for 2005/9/7 and after.

5.3. Predicted and observed Lyα irradiance at the Earth

The computation of the solar Lyα flux, for any direction on the sky from the refined synoptic map is fairly accurate and simple, because detailed radiance observations exist (Lemaire et al., 1978; Fontenla et al., 1988; Curdt et al., 2008). Using data from these sources we tabulate the Lyα radiance, for each solar feature, as function of angle between solar radius and line-of-sight. The Lyα radiance for each feature has a moderate center-to-limb variation that is included in our calculations through this table. The radiance table we used is currently based on observations, but will also be consistent with the current set of models of solar atmospheric features (Fontenla et al., in preparation), because the models are being constructed to fit the observations. A calibration factor is applied to account for the differences in radiometric calibrations of the various instruments. This factor is determined by comparing the computed Lyα irradiance to that observed by SORCE/SOLSTICE (see McClintock et al., 2005; Snow et al., 2005) at the beginning of the forecast period (i.e. on 2005/9/3) over the 121–122 nm bandpass.

Fig. 7 shows the Lyα irradiance observed by SOLSTICE (see http://lasp.colorado.edu/lisird) compared with our prediction using the refined synoptic map in Fig. 6. Fig. 7 shows that the separation between the minima just before and after 2005/9/3 is about 22 days and substantially shorter than the standard solar rotation period. From our analysis it is clear that this separation does not reflect solar rotation only, but is substantially affected by the sudden turn-on of SG1 and by the decay of SG3. The figure also shows the SWAN forecasted irradiance on 2005/9/4, using the method by Quémerais and Bertaux (2000). The web-published SWAN forecast had to be adjusted by a multiplicative constant of 0.99 to match the SORCE/

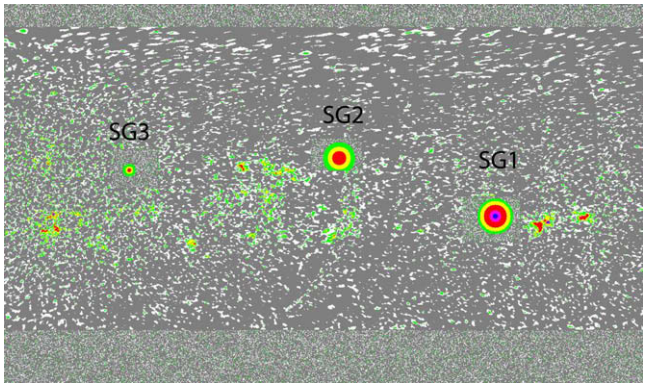

Fig. 6. Refined synoptic map for 2005/9/3 based on synoptic map in Fig. 2, the far-side helioseismic images from GONG (Fig. 3), and the Lyα backscattered flux from SWAN (Fig. 4). This map corresponds to the forecasted features as they will become visible after 2005/9/7. The color codes are the same as in Figs. 1 and 2, and are identified in Table 1.

Please cite this article in press as: Fontenla, J.M., et al. Solar irradiance forecast and far-side imaging. J. Adv. Space Res. (2009), doi:10.1016/j.asr.2009.04.010

SOLSTICE data radiometric calibration at the beginning of the forecast. Finally, the figure shows that the forecast produced by the scheme described here provides much better results than any previous techniques. This is because the method we have introduced combines very specific information on activity centers on the solar surface (including their evolution trends while they were last visible) with information from the far side obtained by two independent methods, one that provides good localization of strong active regions and the other which provides direct Lyα flux. Indeed, the rise of the irradiance is very well reproduced except near peak irradiance, during days 19 and 20 from the start of the forecast (where perhaps the forecast based on Quémerais and Bertaux (2000) alone performs better). The error on days 19 and 20 from our current method likely result from our present neglect of the evolution of regions less important than the major ones we targeted (i.e. SG1, 2, and 3).

6. Discussion and summary

We have developed a significantly improved technique for forecasting XUV/EUV/UV irradiance on a time scale of 7–20 days. The method takes advantage of complementary information provide by helioseismology and Lyα backscatter to include an appraisal of activity developing on the Sun's far hemisphere. Helioseismic maps of the Sun's far surface tell us the location and strength of large active regions. The Lyα backscatter gives us valuable information on the radiance of the regions in question, and also on the radiance of weaker regions not detected by helioseismology. This is the first irradiance forecasting technique that has taken significant advantage of realistic information on far-side solar activity. The development of these resources for irradiance forecasting is therefore in its relative infancy.

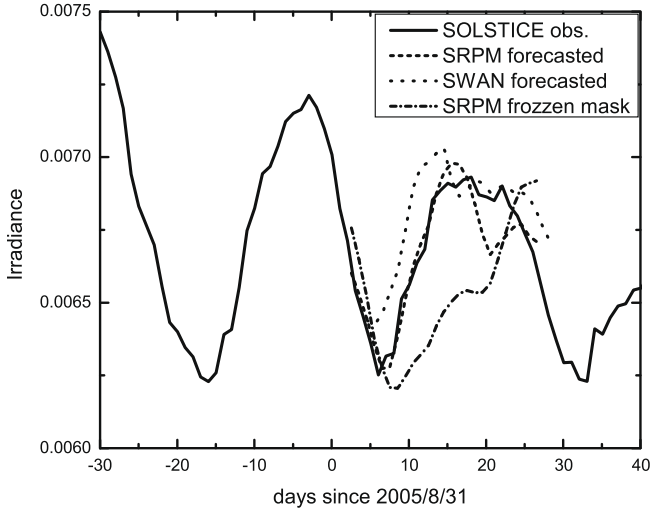

Fig. 7. Lyα irradiance at 1 AU measured by the SORCE/SOLSTICE instrument (solid line) compared with the forecast from the refined synoptic map shown in Fig. 6 (dashed line). Also shown are: (1) the forecast from SWAN made on 9/4 (dotted line), and (2) the irradiance resulting from the synoptic map without refinement shown in Fig. 2 (dot-dashed line).

Further enhancements in irradiance forecasting would certainly accrue from improvements in Lyα backscatter observations and analysis and from advances in far-side helioseismology. The sudden emergence of strong submerged active regions to the Sun's near surface now imposes the major uncertainty in irradiance forecasting. The prospect of forecasting the emergence of submerged active regions is a major object of helioseismology from the *Solar Dynamics Observatory*, scheduled for launch in late 2009, and the ongoing GONG Project in solar activity cycle 24. Our irradiance-forecasting method is designed with the flexibility to take advantage of these new developments.

Nowcasting the spectral solar irradiance (SSI) based on solar-features maps was described in Fontenla et al. (1999), where a set of solar features atmospheric models was introduced. These models are now being improved by more comprehensive data currently available, e.g., Fontenla et al. (2007). Using the SSI nowcast method it is possible to apply the results to a determination of the photoionization of the interplanetary medium and thereby improve the fit used for the SWAN data interpretation. Furthermore, using the techniques presented here, we can now perform forecasting of the SSI at most wavelengths in the EUV/FUV, visible, and infrared. From the forecast of the synoptic maps of solar features on the solar surface, and the models currently in preparation for matching the FUV/EUV spectral radiance of each feature, we plan to construct SSI forecasts for these spectral ranges. This provides a very important resource for forecasts of the thermospheric neutral density and for the degree of ionization of the terrestrial ionosphere as well as for other planets and the interplanetary medium. Using our SSI forecast in the Earth atmospheric models that can take detailed SSI input, satellite drag and communications forecasts can be substantially improved.

Acknowledgments

This work was supported by NASA Contract NAS5-97045 and AFOSR Contract NNX07AO75G at the University of Colorado.

We thank two anonymous referees for very helpful comments.

References

Bertaux, J.-L., Blamont, J.E. A&A 11, 200, 1971.

Bertaux, J.-L., Kyrölä, E., Quémerais, E., Pellinen, R., Lallement, R., Schmidt, W., Berthé, M., Dimarellis, E., Goutail, J.P., Taulemesse, C., Bernard, C., Leppelmeier, G., Summanen, T., Hannula, H., Huomo, H., Kehlä, V., Korpela, S., Leppälä, K., Strömmer, E., Torsti, J., Viherkanto, K., Hochedez, J.F., Chretiennot, G., Peyroux, R., Holzer, T. SoPh 162, 403, 1995.

Braun, D.C., Duvall Jr., T.L., Labonte, B.J. ApJ 335, 1015, 1988.

Bumba, V., Howard, R. ApJ 141, 1492, 1965.

Curdt, W., Tian, H., Teriaca, L., Schule, U., Lemaire, P. A&A 492, L9, 2008.
Fontenla, J., Harder, J. MmSAI 76, 826–833, 2005.
Fontenla, J.M., Reichmann, E.J., Tandberg Hanssen, E. ApJ 329, 464–481, 1988.
Fontenla, J.M., White, O.R., Fox, P.A., Avrett, E.H., Kurucz, R.L. ApJ 518, 480–499, 1999.
Fontenla, J., Balasubramaniam, K.S., Harder, J. ApJ 667, 1243–1257, 2007.
Fuller-Rowell, T., Solomon, S., Roble, R., Viereck, R. Solar variability and its effects on climate, Geophys. Monograph 141, American Geophysical Union, 2004.
González Hernández, I., Hill, F., Lindsey, C. ApJ 669, 1382, 2007.
Lemaire, P., Charra, J., Jouchoux, A., Vidal-Madjar, A., Artzener, G.E., Vial, J.C., Bonnet, R.M., Skumanich, A. ApJ 223, L55, 1978.
Lindsey, C., Braun, D.C. ApJ 485, 895, 1997.
Lindsey, C., Braun, D.C. Science 287, 1799, 2000a.
Lindsey, C., Braun, D.C. SoPh 192, 261, 2000b.
McClintock, W.E., Rottman, G.J., Woods, T.N. SoPh 230, 225, 2005.
Ortiz, A., Rast, M. MmSAI 76, 1018, 2008.
Quémerais, E., Bertaux, J.-L. GRL 29, 1018, 2000.
Quémerais, E., Lallement, R., Ferron, S., Koutroumpa, D., Bertaux, J.-L., Kyrl, E., Schmidt, W. JGRA 111, A09114, 2006.
Rast, M.P., Ortiz, A., Meisner, R.W. ApJ 673, 1209, 2008.
Snow, M., McClintock, W.E., Rottman, G., Woods, T.N. SoPh 230, 295, 2005.
Thomas, G.E., Krassa, R.F. A&A 11, 218, 1971.

Please cite this article in press as: Fontenla, J.M., et al. Solar irradiance forecast and far-side imaging. J. Adv. Space Res. (2009), doi:10.1016/j.asr.2009.04.010